Revealing the role of the 1T phase on the adsorption of organic dyes on MoS₂ nanosheets†

Asmaa M. Omar,[a] Ossama I. Metwalli,[a] Mohamed R. Saber,[b] Gomaa Khabiri,[a] Mohamed E. M. Ali,[c] Arafa Hassen,[a] Mostafa M. H. Khalil, [iD][d] Ahmed A. Maarouf*[e] and Ahmed S. G. Khalil [iD] *[a]

Herein, different phases of MoS₂ nanosheets were synthesized, characterized and tested for dye removal from water. The influence of the MoS₂ phases as well as the 1T concentration on the adsorption performance of organic dyes MO, RhB and MB was deeply investigated. The results revealed that the 1T-rich MoS₂ nanosheets have superior adsorption performance compared to other 2H and 3R phases. The kinetic results of the adsorption process demonstrate that the experimental data followed the pseudo-second order equation. Meanwhile, the adsorption of dyes over the obtained materials was fitted with several isotherm models. The Langmuir model gives the best fitting to the experimental data with maximum a adsorption capacity of 787 mg g⁻¹. The obtained capacity is significantly higher than that of all previous reports for similar MoS₂ materials. Computational studies of the 2H and 1T/2H-MoS₂ phases showed that the structural defects present at the 1T/2H grain boundaries enhance the binding of hydroxide and carboxyl groups to the MoS₂ surface which in turn increase the adsorption properties of the 1T/2H-MoS₂ phase.

1. Introduction

Two-dimensional (2D) layered materials have attracted attention for a wide range of applications including hydrogen evolution,[1] adsorption,[2,3] photocatalysis,[4,5] lithium ion batteries,[6] and supercapacitors.[7–9] Among the different types of 2D materials, molybdenum disulfide (MoS₂) has been one of the most studied materials over the last few years.[10,11] MoS₂ can exist in three phases; two are semiconducting and stable (hexagonal, 2H, and rhombohedral, 3R) and the third (1T) is metallic with a trigonal structure. The 1T phase is metastable and can be transformed into the 2H phase after thermal treatment.[12,13] The 1T-MoS₂ phase was found to be a superior catalyst due to the high carrier mobility, higher hydrophilicity and abundant active sites, not only at the edges of the nanosheets but also within the basal plane of the 1T phase.[14–16] Recent studies have shown that the 1T and 2H phases coexist in single layers of hybridized MoS₂ (ref. 17–19) with 1T-phase concentration up to 70%.[5,18]

Treatment of organic pollutants using MoS₂ materials *via* adsorption or photocatalytic degradation has been extensively studied.[1–4,6,7,12,20] However, several contradicting reports on this topic can be found due to the very delicate nature of the material.[1–4,6–9] The electronic structure of the material and its activity are quite sensitive to several parameters including the molybdenum local coordination, surface defects, crystal phase, degree of exfoliation, and the size and morphology of the nanosheets. For instance, several reports claimed fast and efficient adsorption of different organic dyes using MoS₂ composites.[1–4,6,21–28] He Li *et al.*[29] used porous MoS₂ nanosheets to efficiently remove RhB, MB and MO with adsorption capacities of about 163.0 mg g⁻¹, 499.0 mg g⁻¹ and 125.1 mg g⁻¹ at 420 min, respectively. Also, Xiu and co-workers[21] found that the MoS₂ exhibits good and fast performance for removal of MB from aqueous solution, with an adsorption capacity of 146.43 mg g⁻¹ in 6 min. However, in another study the authors reported no adsorptive capabilities for their MoS₂ samples.[20] Xie and co-workers[30] reported low adsorption towards MB and MO with adsorption capacity of about 70 and 25 mg g⁻¹ respectively.

The high adsorption capacity reported for some MoS₂ nanosheets and MoS₂ based heterostructures were ascribed to the high surface area of MoS₂ and MoS₂-composites, which increases the number of active sites per unit volume and consequently leads to high adsorption capacity.[31] However, in other studies,[7,32] it has been demonstrated that the surface

[a]Environmental and Smart Technology Group (ESTG), Physics Department, Faculty of Science, Fayoum University, 63514 Fayoum, Egypt. E-mail: asg05@fayoum.edu.eg
[b]Chemistry Department, Faculty of Science, Fayoum University, 63514 Fayoum, Egypt
[c]Water Pollution Research Department, National Research Centre, 33 El Bohouth St. P.O. 12622, Giza, Egypt
[d]Chemistry Department, Faculty of Science, Ain Shams University, Abbassia 11566, Cairo, Egypt
[e]Department of Physics, IRMC, Imam Abdulrahman Bin Faisal University, Saudia Arabia. E-mail: amaarouf@iau.edu.sa
† Electronic supplementary information (ESI) available. See DOI: 10.1039/c9ra05427h

area has no effect on the adsorption activity. Whereas an effect of intermolecular interaction, such as van der Waals and electrostatic attraction,[7] or the existence of highly reactive OH radical groups on the MoS_2 surface[33] was proposed. To the best of our knowledge, there are no reports that provide a clear correlation between the high adsorption performance of MoS_2 with the material surface activity and its phase composition.

Computational studies of the adsorption properties of two-dimensional materials have been extensively performed, so as to understand the role of various parameters controlling molecular adsorption on their surfaces. Graphene, being a 2D material with relative ease of fabrication was extensively studied.[34–36] The surface structure, defects, and functionalization play an important role. In addition, various properties of the adsorbents (such as geometrical configuration, hydrophobicity, size, and substituent chemical groups) were investigated.[37,38]

With the progress in fabricating 2D MoS_2 nanosheets, molecular adsorption on its surface have been recently computationally investigated, where defects arising from Mo or S vacancies can lead to an enhancement of its adsorption and catalytic properties.[39,40] Edges of MoS_2 nanoparticles, where the atomic coordination of the Mo and S atoms is different from the bulk, provide active sites that can anchor various functional groups, adsorb various gases, and catalyse hydrogen evolution reactions.[33,41,42] Mixed phase 1T/2H structures have been experimentally and computationally studied for various applications, including solar thermal water purification.[43] The 1T/2H in plane phase hybridization offers a MoS_2 structure with lower sheet resistance (<1 kΩ sq^{-1}) and high specific capacitance two orders of magnitude higher than the pure 2H phase.[44] Electronic studies of hybridized phases revealed that the presence of 1T islands in a 2H MoS_2 sheet induces some structural defects at the grain boundaries of the 1T phase, where the S and Mo sublattices suffer some local stresses. These manifests themselves as changes in the 2H electronic spectrum, leading to the emergence of midgap states, and causing an increase in the electronic conductivity of the hybrid phase compared to the pure 2H one. In addition, the structural defects at the 1T boundary alter the electrostatic landscape of the system, inviting an investigation of molecular adsorption in these regions.

In our recent work,[5] hybridized phases of MoS_2 were synthesized using hydrothermal method with the reactor filling ratio acting as the controlling factor of the 1T content of the material. The results of the photocatalytic degradation of MO using these materials under visible light strongly correlated the photocatalytic activity of MoS_2 materials to their phases with a significantly improved performance of 1T containing phases. Our calculations suggested that the introduction of 1T sites into the 2H layers of the material lead to surface distortions and mid-gap states which improve the conductivity and catalytic activity.

In this report, the adsorptive properties of the mixed phase MoS_2 nanosheets (1T/2H, 2H and 3R) have been explored. The adsorption behaviour of the samples has been thoroughly investigated using MB, RhB and MO organic dyes in order to

determine the effect of the sample phase on the adsorption performance. The conditions of adsorption process have been optimized in order to conduct detailed kinetics and thermodynamics studies. We also present first principle calculations of the adsorption properties of the different phases of MoS_2 nanosheets, where we study the effects of the 1T/2H domain boundaries.

2. Experimental

2.1 Chemicals

Methylene blue (MB); ($C_{16}H_{18}ClN_3S$), methyl orange; (MO) ($C_{14}H_{14}N_3NaO_3S$) and rhodamine B (RhB); ($C_{28}H_{31}ClN_2O_3$) were purchased from Sigma Aldrich. Ammonium molybdate ((NH_4)$_6Mo_7O_{24}\cdot4H_2O$) was purchased from SD Fine Chem limited, India. Thiourea (CH_4N_2S) was purchased from Loba Chemie, India. All chemicals were of analytical grade and used without further purification. The different concentrations of MB, MO, and RhB solutions were prepared by dissolving the required amount of these dyes in deionized water.

2.2 Synthesis of MoS₂

Four different samples (S1–S4) of MoS_2 nanosheets were prepared using the hydrothermal method. For S1, 2.47 g of (NH_4)$_6Mo_7O_{24}\cdot4H_2O$ and 0.76 g of CS (NH_2)$_2$ were dissolved in 60 mL of DI water under constant stirring. The whole mixture was transferred into a 134 mL Teflon-lined stainless-steel autoclave. The autoclave was kept in an oven at 200 °C for 24 h, then left to cool down to room temperature. The resulting black precipitate was collected by centrifugation, washed three times with distilled water then with ethanol, and dried in an oven for 12 h at 80 °C. To obtain the different phases, a variation of the reactor filling ratio (75%, S2) and molar ratio of Mo and S 1 : 25, 75% (S3) were used. Further thermal treatment of 1T/3R-MoS_2 in a tube furnace (Carbolite) at 800 °C under Ar for 2 hours resulted in 2H-MoS_2 (S4). The ratios between IT and 2H/3R phases in the samples were estimated from XPS analyses.[5]

2.3 Materials characterization

The morphologies of the prepared samples were measured using scanning electron microscope (Zeiss Sigma 500 VP, equipped with Oxford EDS detector). HRTEM images were obtained using JOEL 2100F at 200 kV. X-ray diffraction patterns were collected using Cu Kα monochromatic radiation (K$_{1/4}$ 1.54056) at room temperature on a 202964 Panalytical Empryan diffractometer. Brunauer–Emmet–Teller (BET) surface area was analysed using a TriStar instrument with nitrogen adsorption at 77 K using the Barrett–Joyner–Halenda (BJH) method. The zeta potential and size at different pH was performed using Nano-ZS (Malvern, UK).

2.4 Adsorption experiments

The adsorption experiments were performed in the dark at room temperature in order to eliminate any possible

photocatalytic degradation of the used dyes. The adsorption behaviour of the prepared samples was investigated by monitoring the reduction of MB, RhB and MO dyes in aqueous solutions (20 mg L^{-1}). A calculated amount of the MoS$_2$ samples was separately added to the above solutions with continuous magnetic stirring at 800 rpm. During the experiments, 3 mL of the supernatant was taken at different time intervals and analysed by UV-vis spectrophotometer (Agilent, Cary 60) at $\lambda_{max} =$ 664, 554 and 464 nm for MB, RhB and MO respectively, to determine the dye concentration. The sorbent was isolated *via* centrifugation. The adsorption percentage of dyes and adsorption capacity of MoS$_2$ was calculated using the following equations:

$$R(\%) = \frac{C_0 - C_t}{C_0} \times 100 \qquad (1)$$

$$q_t \text{ (mg g}^{-1}) = (C_0 - C_t)V_d/m_A \qquad (2)$$

where, C_0 is the initial concentration of dye; C_t is the dye concentration after t minute; V_d is the volume of dye solution; m_A is the weight of MoS$_2$.

2.5 Computational methods

All calculations were performed using the Quantum Espresso plane waves package based on density functional theory.[45] The generalized gradient approximation was used in the scheme of Perdew–Burke–Ernzerhof for the exchange correlation functional, with ultrasoft pseudopotentials. A 6 × 6 2H supercell was constructed, with a vacuum separation of 13 Å, to prevent the interaction between neighboring cells. All studied systems were structurally relaxed, until all atomic forces become less than 0.0001 Ry bohr^{-1}. The self-consistent calculations were performed with an energy cut-off of 35 Ry, and with a 2 × 2 × 1 Monkhorst–Pack k-mesh.[46] The adsorption energies, E_{ad}, were calculated according to:

$$E_{ad} = E(MoS_2) + E(X) - E(MoS_2 + X) \qquad (3)$$

where $E(MoS_2)$, $E(X)$, and $E(MoS_2 + X)$ were the total energies of the isolated MoS$_2$ system, the isolated functional group X, and combined MoS$_2$ + X systems.

3. Results and discussion

MoS$_2$ flower-like structures with different 1T concentration were synthesized by hydrothermal reaction between ammonium molybdate and thiourea at 200 °C. The resulting phase is controlled through three factors: the molar ratio of Mo : S, the filling ratio of the reactor, and thermal treatment. Adjusting the ratio of Mo : S to 1 : 5 at 45% filling ratio of the reactor gives the hybridized S1, while the same molar ratio at 75% filling ratio gives S2. By increasing the filling of the reactor to 75% and using excess of sulphur with a Mo : S ratio of 1 : 25 we obtained S3. The thermal treatment of S3 at 800 °C under argon in a tube furnace gave pure 2H phase (S4). The obtained

samples have been characterized using several analytical techniques.[5]

Fig. SI.1† shows the XRD patterns of the synthesized MoS$_2$ samples. All the diffraction peaks of the prepared samples appeared noisy and broad, mainly due to the formation of nanosized MoS$_2$ material.[47] S4 exhibits five diffraction peaks at 13.7°, 33.2°, 39.3°, 49.2°, and 58.6°, defined by the (002), (100), (103), (105), and (110) crystal planes, respectively. These results are in a good agreement with hexagonal 2H-MoS$_2$ pattern (PDF no. 00-024-0513). Whereas the diffraction patterns of S1–S3 indicate the existence of a hybridized 1T/2H and 1T/3R phases.[48] SEM measurements of the MoS$_2$ materials (Fig. 1A) showed micro-flowers consisting of aggregated MoS$_2$ nanosheets for all samples which is typically reported for similar hydrothermally synthesized MoS$_2$ materials.[49] The EDS mapping (Fig. 1B–D) revealed the existence of Mo, S, and O in the layered MoS$_2$ with uniform distribution, confirming the high quality of the prepared MoS$_2$.

Fig. 2A shows the nitrogen adsorption–desorption isotherms curve of S1. The specific surface area of the MoS$_2$ nanosheets, calculated by the multipoint BET method, was 6.18 m^2 g^{-1}. The specific area of the S3 and S4 was found to be 6.67 and 4.48 m^2 g^{-1}, respectively (Fig. SI.2†). No significant differences in the specific areas of the three samples were observed, which suggests that different adsorption responses of the samples cannot be attributed to the surface area of the MoS$_2$ nanosheets. The adsorption of dyes onto the MoS$_2$ adsorbent surface is strongly affected by the surface charge of the adsorbent. In addition, the adsorbent surface charge is significantly influenced by pH value. The zeta potential measurements of S1, S2 and S4 (Fig. 2B) reveal high negative surface charges in the range of pH = 3–10, which reflects the excellent stability of the MoS$_2$ dispersions.

This negative surface charges are mainly due to OH and COOH functional groups on MoS$_2$ surface[50] which act as surface active adsorption sites.[51] The negative charge density on the surface of MoS$_2$ nanosheets suggests that the interaction with adsorbates should be mainly electrostatic in nature with a possible affinity towards cationic dyes.[52,53] Similar charge profiles at different pH were observed for S2 and S4. Fig. 2C shows the particle size of S1, S2 and S4 aqueous dispersions. It can be seen that the MoS$_2$ nanosheets of S1, S2 and S4 have small sizes (131 nm, 127 nm and 123 nm respectively) compared to previous reports.[54] Very likely this is due to the better degree of exfoliation of MoS$_2$ nanosheets.

3.1 Adsorption performance

In order to investigate the adsorption behaviour of the four prepared MoS$_2$ samples with different phases, a certain dose of the samples (50 mg) was added to MB aqueous solution (100 mL, 20 ppm). The experiments were performed under dark conditions for 30 min. Fig. SI.3† shows a removal efficiency of 99% and adsorption capacity 40 mg g^{-1} for S1 (70% 1T) compared to 87%, 34 mg g^{-1} for S2 (20% 1T), 22%, 9 mg g^{-1} for S3 (1T/3R) and 11%, 5 mg g^{-1} for S4 (2H) after 5 min. These results clearly indicate an improved performance of the 1T rich samples over 2H and 3R samples.
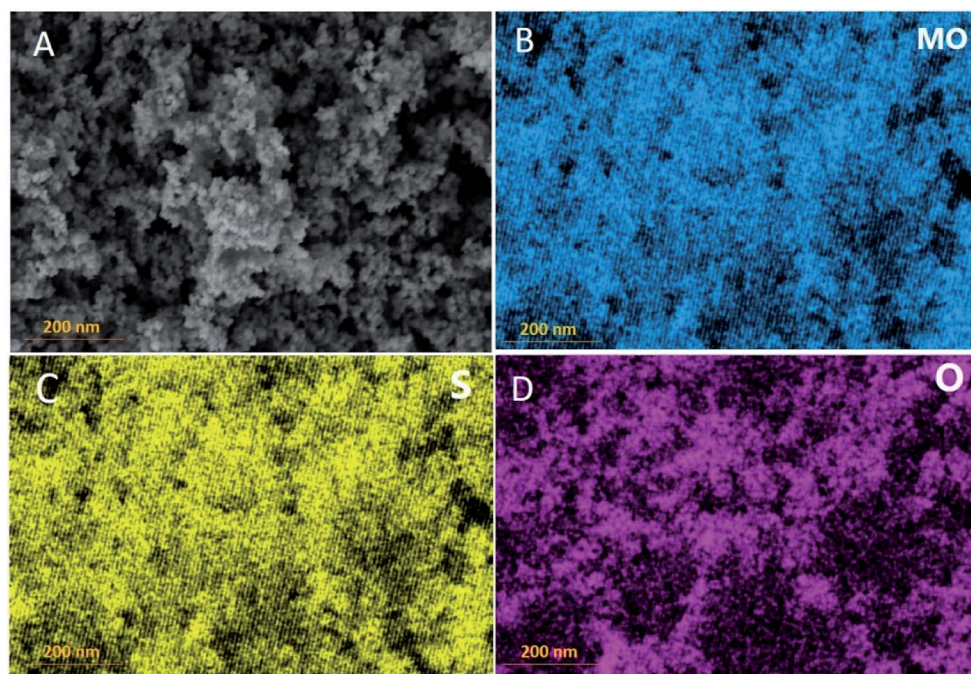
Fig. 1 (A) SEM image of the micro-flowers MoS$_2$ nanosheets, (B–D) EDS elemental mapping of the MoS$_2$ nanosheets.

We investigated the adsorption selectivity of S1 towards different cationic (MB, RhB) and anionic (MO) dyes. The adsorption experiment was carried out for 120 min using 100 ppm dye solutions. The results show a much higher removal percent (adsorption capacity) of cationic dyes; MB, 99% (201 mg g^{-1}), and RhB, 77% (160 mg g^{-1}) as compared to
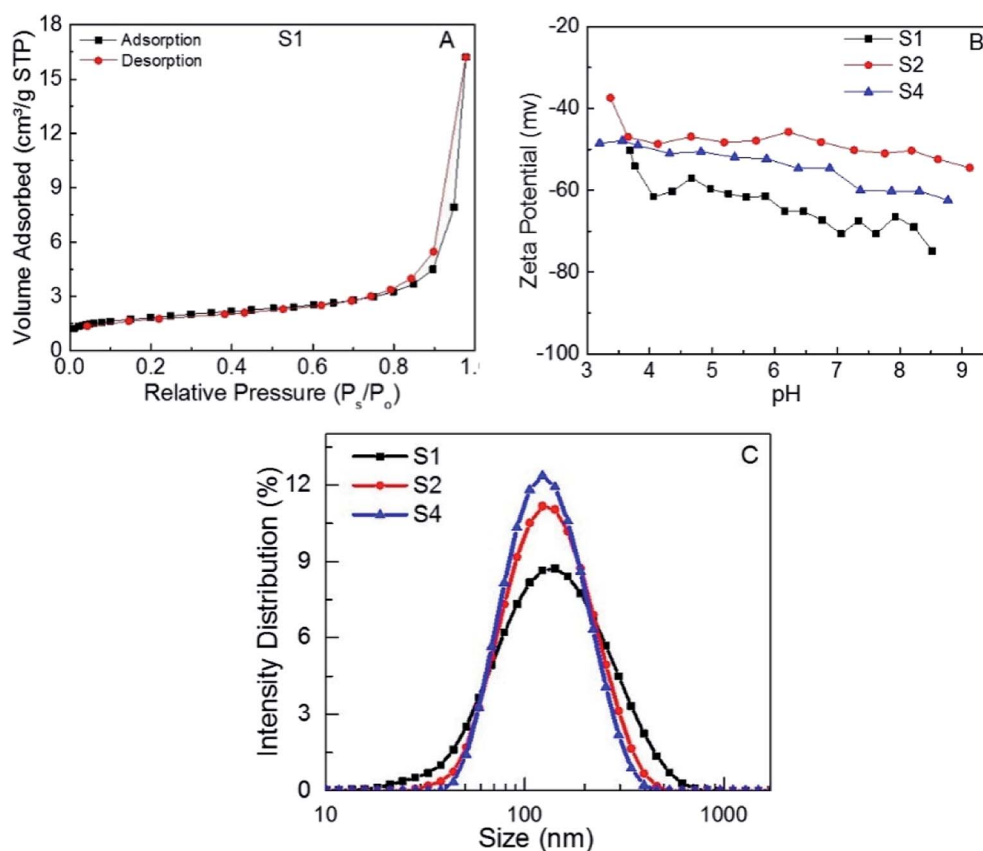

Fig. 2 (A) Nitrogen adsorption–desorption isotherms, (B) zeta potential of S1 at different pH values, (C) particle size distribution of S1, S2 and S4 aqueous dispersions.
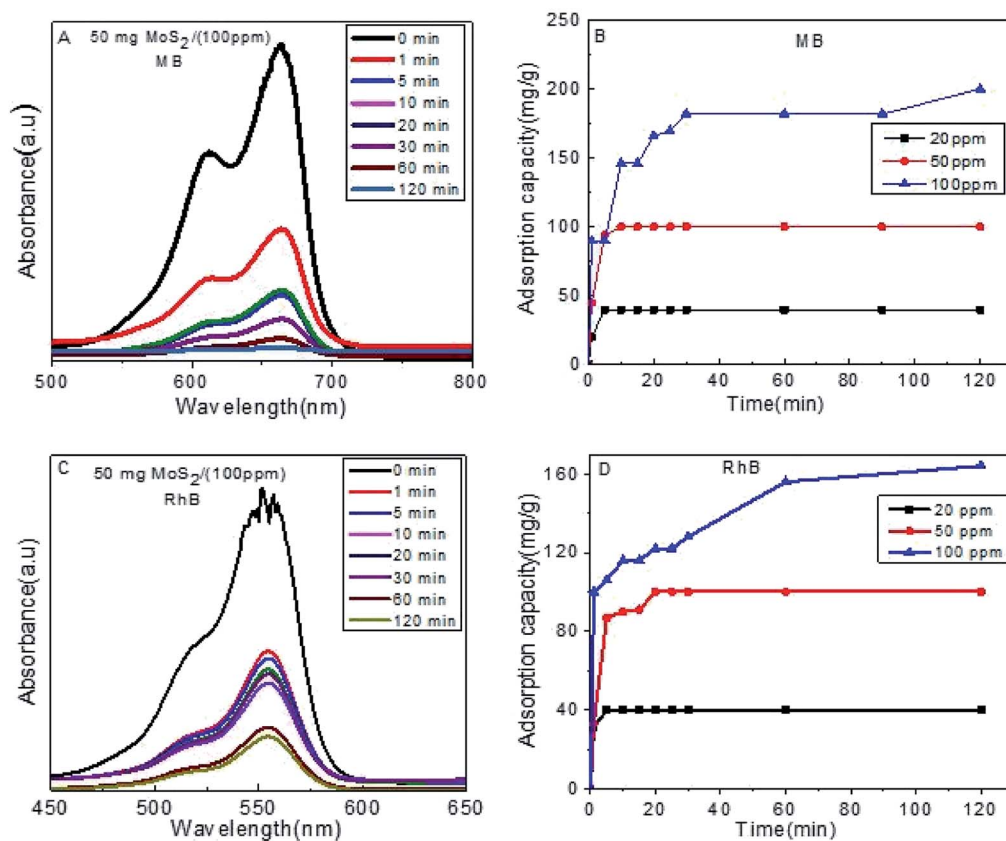
Fig. 3   (A) Absorption efficiency of MB on S1, (B) adsorption capacity for MB, (C) absorption efficiency of RhB on S1, (D) adsorption capacity for RhB.
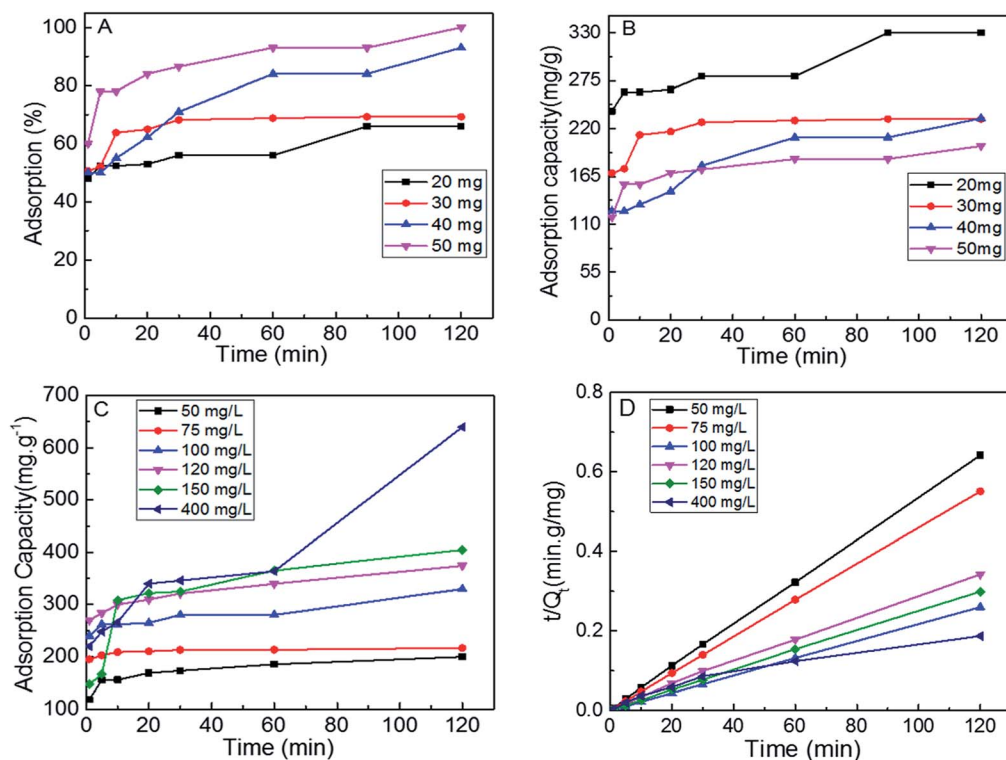

Fig. 4   (A and B) adsorption performance of different doses of S1 for MB aqueous solution, adsorption capacity (C) and pseudo second order model fits (D) of S1 at different dye concentrations.

Table 1 Parameters of different isotherms for adsorption of MB onto S1

Models	Parameter	Value
Pseudo second order model, Langmuir: $C_e/q_e = 1/K_L Q_0 + C_e/Q_0$	K_2 (g mg^{-1} min^{-1})	9×10^{-4}
	q_e (mg g^{-1})	636
	R^2	0.966
	Q_0 (mg g^{-1})	787
	K_L (L mg^{-1})	0.0179
	R_L	0.1223–0.527
	R^2	0.9899
Freundlich: $\ln q_e = \ln K_F + (1/n) \ln C_e$	$1/n$	0.4129
	K_F (L mg^{-1})	67.424
	R^2	0.9954
Temkin: $q_e = B_1 \ln K_T + B_1 \ln C_e$	B_1	154.84
	K_T	0.2235
	R^2	0.9795
Dubinin and Radushkevich: $\ln q_e = \ln Q_s - B\varepsilon^2$	Q_s (mg g^{-1})	470.69
	K	3×10^{-5}
	R^2	0.77

anionic (MO), 23% (50 mg g^{-1}) (Fig. SI.4A and B†). These results are in good agreement with the negative surface charge indicated by the zeta potential measurements (Fig. 2C). They are also in good agreement with the previous reports that indicated a greater affinity of MoS$_2$ sorbents towards cationic dyes.[24,25,48,55,56]

To evaluate the adsorption capacity of as-prepared S1 towards MB and RhB, a 50 mg dose was added to aqueous solution of different concentrations (20 ppm, 50 ppm and 100 ppm) (Fig. 3). Complete removal was obtained after 120 min with an improved capacity for MB than RhB, which could be attributed to its smaller molecular size.

In order to determine the optimum conditions to conduct further adsorption studies, the S1 dosage was varied from 50 mg to 20 mg. Fig. 4A and B show the percent adsorption and adsorption capacity of the S1 for MB (100 ppm) at varying
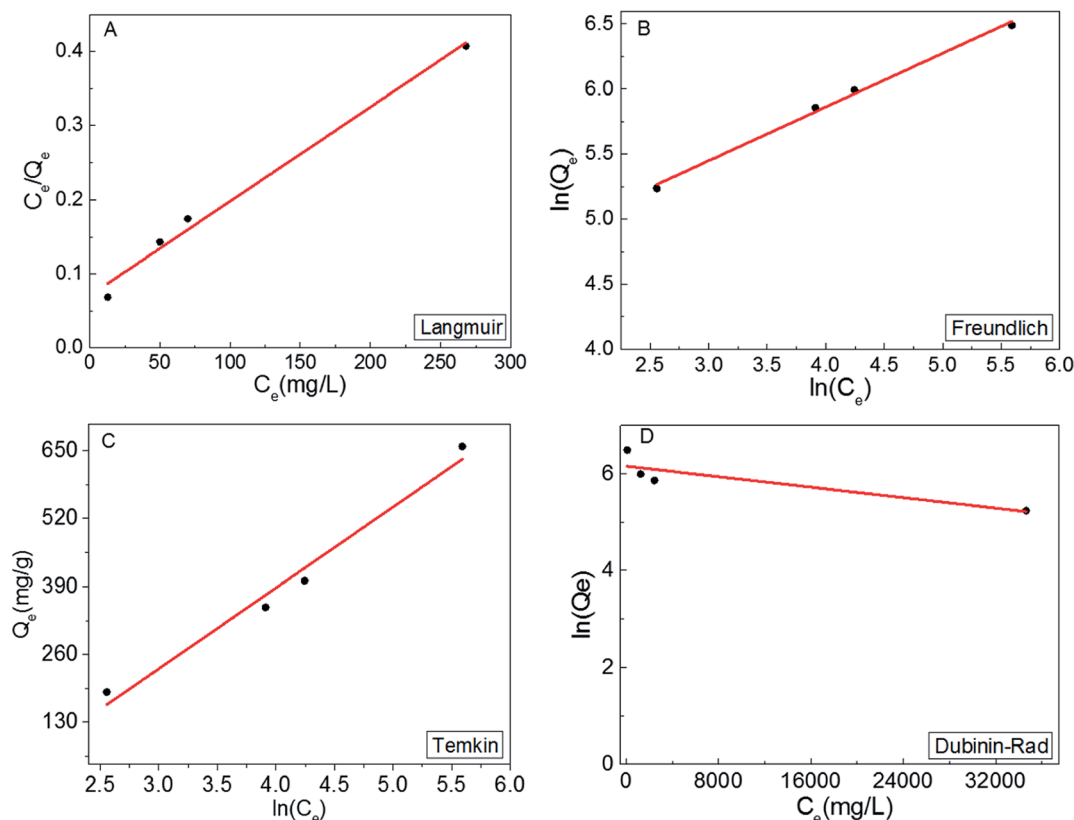

Fig. 5 Langmuir (A), Freundlich (B), (C) Temkin and (D) Dubinin–Rad isotherm curves fitting for MB adsorption onto S1.

adsorption times. As the MoS$_2$ dosage decreased from 50 to 20 mg, the adsorption capacities increased from 200 mg g^{-1} to 330 mg g^{-1}. When the dye concentration was further increased up to 400 mg L^{-1}, adsorption capacity of 652 mg g^{-1} was achieved (Fig. 4C).

The kinetics of the adsorption process was investigated by fitting the data to different kinetic models including pseudo first and second order models. Such models provide detailed information on the adsorption mechanism and the type of adsorption processes involved, including diffusion control, chemical reaction, and mass transport processes.

The kinetics studies for MB onto S1 was investigated using pseudo-first order and pseudo-second order, which can be expressed as:[57]

$$\ln(q_e - q_t) = \ln q_e - K_1 t \tag{4}$$

$$\frac{t}{q_t} = \frac{1}{K_2 q_e^2} + \left(\frac{1}{q_e}\right) t \tag{5}$$

where K_1, K_2 are the pseudo-first and pseudo-second order rate constants (g mg^{-1} min^{-1}). q_t and q_e are the amounts adsorbed at time t and at equilibrium (mg g^{-1}) respectively. Our experimental data were fit against pseudo-first and
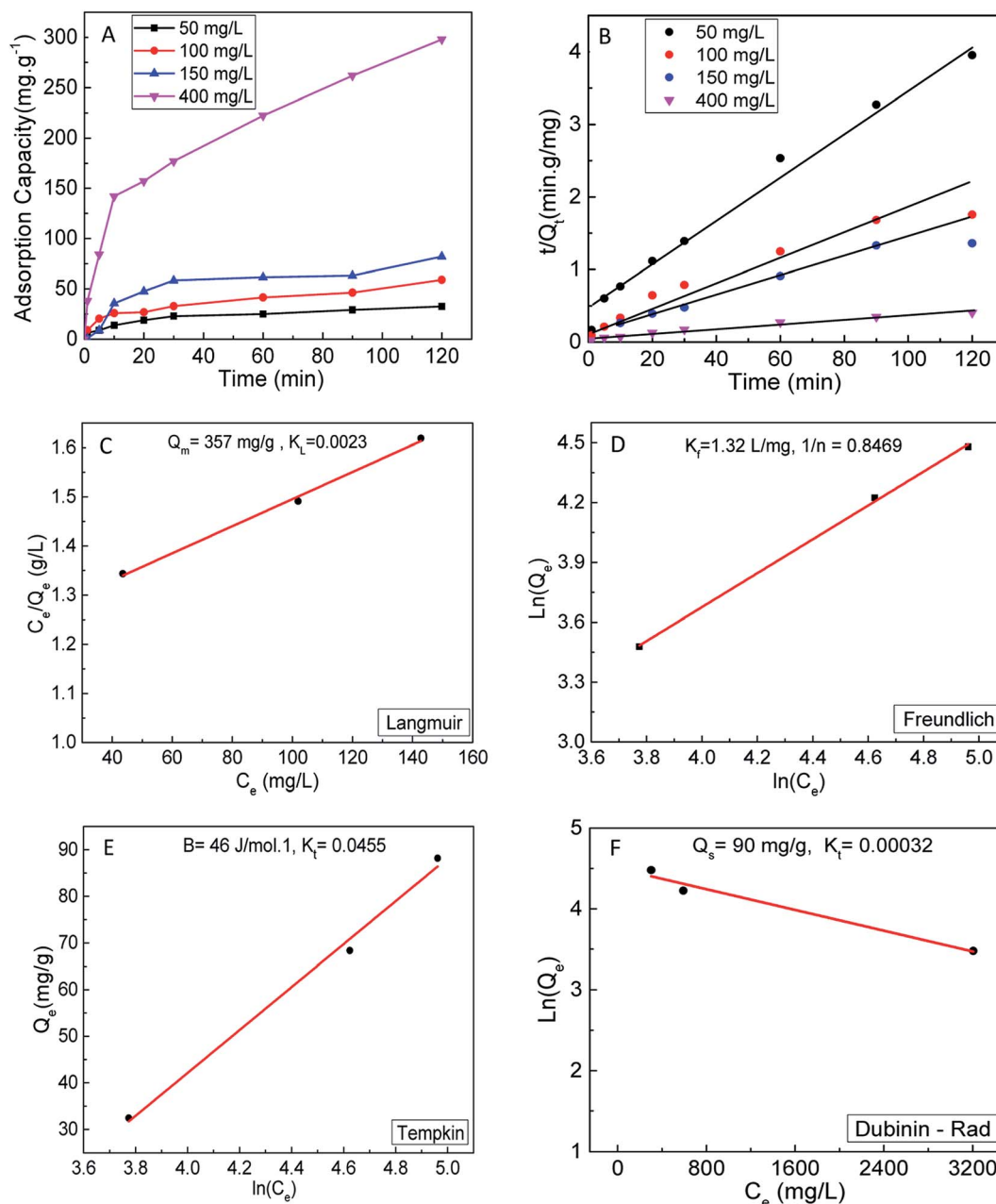

Fig. 6 Adsorption performance of S2; (A) adsorption performance of different concentration of MoS$_2$ for MB aqueous solution, (B) pseudo second order model fits, (C) Langmuir (D), Freundlich (E) Temkin and (F) Dubinin–Radushkevich isotherm curve fitting for MB adsorption onto S2.

Table 2 Adsorption capacity of recent reports on MoS_2 and MoS_2-based materials

Materials	Phase	Adsorption capacity (mg g^{-1})	Dye	Ref.
MoS_2	Hexagonal	146.43	MB	21
MoS_2	No specified, but based on XRD shown it is hexagonal	297	MB	23
MoS_2	Hexagonal	499	MB	29
MoS_2	Hexagonal	208	MB	50
		291	RhB	
MoS_2–TiO_2	Hexagonal	364.56	MB	60
MoS_2	Hexagonal	343.74	MB	61
g-MoS_2-decorated biochar	Hexagonal	249.45	Tetracycline hydrochloride (TC)	62
Ni/MoS_2	Cubic	277.77	Congo red (CR)	22
MoS_2	Hexagonal	161.29	Crystal violet dye (CV)	63
MoS_2	Hexagonal	49.2	RhB	7
MoS_2	S1 70% 1T-MoS_2	787	MB	Our work
	S2 20% 1T-MoS_2	357		

second order. Fig. SI.5† shows that the pseudo-first-order didn't give a good fit for the experimental data. R^2 was very low (0.5519) and q_e was 445 mg g^{-1} for 400 mg L^{-1} dye which was far below the experimental value of q_e (652 mg g^{-1}). As shown in Fig. 4D, acceptable correlation was only observed for the pseudo-second order. The fit resulted in q_e values (*e.g.* 636 mg g^{-1} at 400 mg L^{-1} dye, *cf.* Table 1) was in excellent agreement with the experimental value (652 mg g^{-1}). These collective results indicated that the adsorption process, to large extent depends on the surface active sites induced by the 1T interfaces.[58]

3.2 Isotherms

In order to obtain a deeper insight on the nature of the adsorption layer and the distribution of the active sites on the sorbent surface, the adsorption data were fit to the following isotherms:

Langmuir isotherm which is expressed as:[59]

$$\frac{C_e}{q_e} = \frac{1}{K_L Q_0} + \frac{C_e}{Q_0} \tag{6}$$

$$R_L = \frac{1}{(1 + K_L C_0)} \tag{7}$$

where Q_0 and K_L are Langmuir constants. C_0 and R_L are the intimal concentration and separation factor. The correlation coefficient R^2 (0.9899) indicates that the adsorption process fits Langmuir model (Fig. 5A) with a maximum adsorption capacity (Q_0) of 787 mg g^{-1} (Table 1). The separation factor R_L is between 0 and 1, which indicates that the adsorption process is quite favourable.
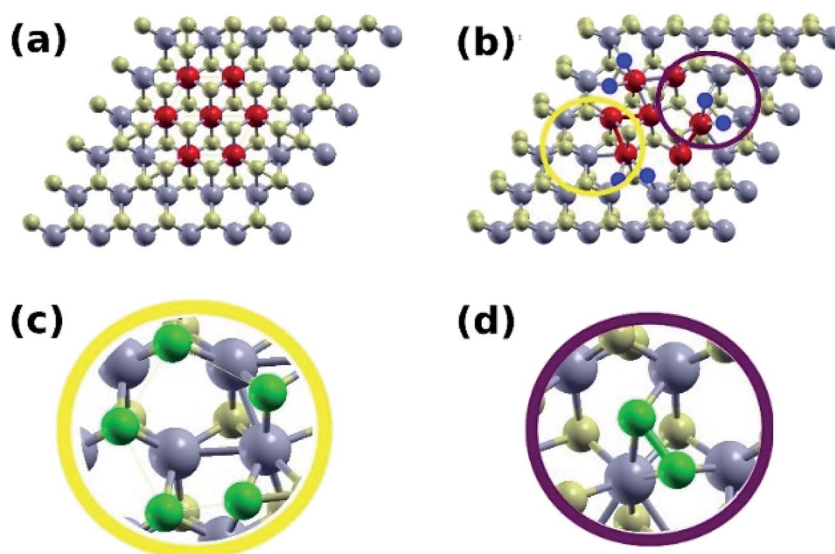

Fig. 7 (a) The 6 × 6-unit cell of an unrelaxed MoS_2 1T/2H mixed phase system where red Mo atoms indicate the 1T phase. (b) Unit cell after relaxation. The yellow circle indicates a region with no S atoms. The purple circle surrounds bonded S atoms. (c and d) A zoom-in on the two aforementioned regions, with the S atoms shown in green.
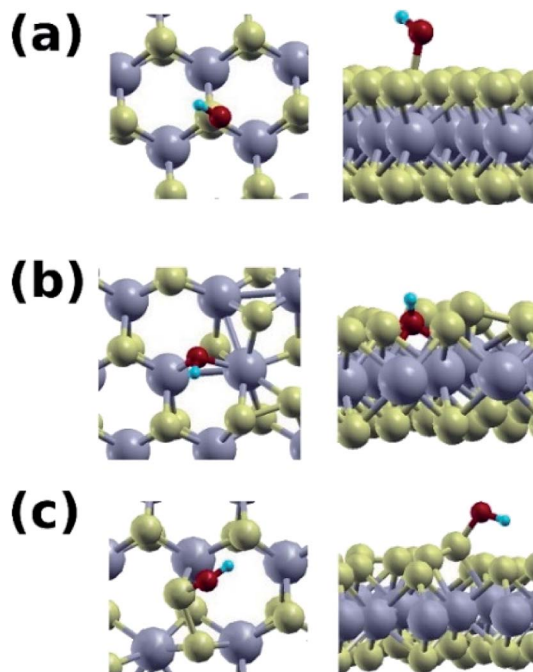
Fig. 8 (a) Top and side views of the OH group adsorbed at the S site of the pure 2H phase. (b) Top and side views of the OH group adsorbed at one of the Mo atoms at the boundary between the 2H and 1T phases. (c) Top and side views of the OH group adsorbed at a S site at the boundary between the 2H and 1T phases.

Freundlich isotherm model[30] was used to evaluate the heterogeneity of the sorbent surface and can be expressed as follow:
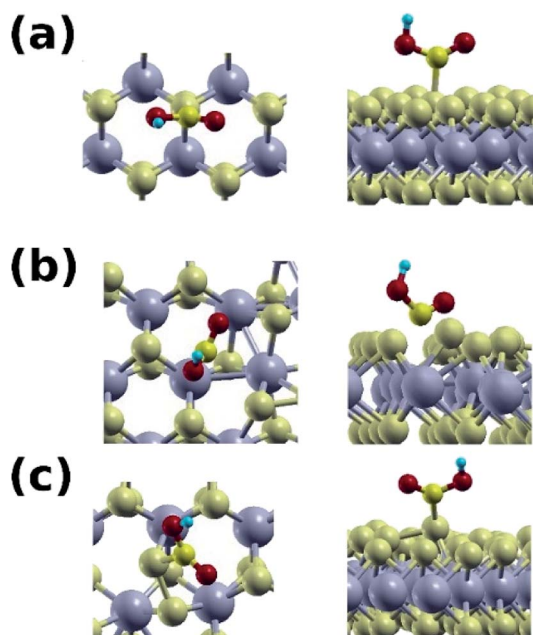

Fig. 9 (a) Top and side views of the COOH group adsorbed at the S site of the pure 2H phase. (b) Top and side views of the COOH group adsorbed at one of the Mo atoms at the boundary between the 2H and 1T phases. (c) Top and side views of the COOH group adsorbed at a S site at the boundary between the 2H and 1T phases.

$$\ln q_e = \ln K_F + \frac{1}{n}\ln C_e \tag{8}$$

where K_F is adsorption capacity at unit concentration and $1/n$ is adsorption intensity. The plot of Freundlich model is shown in Fig. 5B. The $1/n$ value of 0.4129 indicates a favourable adsorption process.[58]

Temkin isotherm model can be expressed as follows:

$$q_e = B_1 \ln K_T + B_T \ln C_e \tag{9}$$

$$B_1 = \frac{RT}{b} \tag{10}$$

where K_T is the equilibrium binding constant (L mg^{-1}), and B_1 is related to the heat of adsorption. T is the absolute temperature in K, R is the universal gas constant. The high correlation coefficient (Fig. 5C) implies that the heat of adsorption of all the dye molecules decreases with increasing coverage.

For Dubinin–Radushkevich isotherm model:[59]

$$\ln q_e = \ln Q_s - K\varepsilon^2 \tag{11}$$

$$\varepsilon = RT \ln\left(1 + \frac{1}{C_e}\right) \tag{12}$$

where, K is a constant related to the adsorption energy, Q_s is the theoretical saturation capacity and ε is the Polanyi potential. This model describes the sorbent characteristics and free energy transported from the molecules to the surface, however, a poor correlation was observed (Table 1). The plot of Dubinin–Radushkevich model was shown in Fig. 5D.

It can be concluded from the above results that the high correlation coefficient to Langmuir, Freundlich and Temkin isotherms suggest that several sorption mechanisms are involved.[58] Moreover, the obtained results revelled that the surface of MoS_2 exhibits a blend of heterogenous and homogenous active sites, and the overall rate of adsorption of MB on MoS_2 surface was achieved by the two isotherm mechanisms.

To further investigate the role of surface-active sites in the adsorption process, the adsorption kinetics and isotherms of S2 were also investigated. The adsorption kinetics are shown in Fig. 6A and B, which indicates that the experimental data are fit with the pseudo-second-order model. The adsorption data were fit to the same isotherm models (Fig. 6C–F). The results clearly show a lower adsorption capacity (357 mg g^{-1})

Table 3 Adsorption energies and bond lengths of the OH and COOH groups at different adsorption sites

OH	E_b (eV)	O–S (Å)	O–Mo (Å)
2H	1.26	1.79	—
1T/2H_S	2.66	1.67	—
1T/2H_Mo	2.95	—	2.09

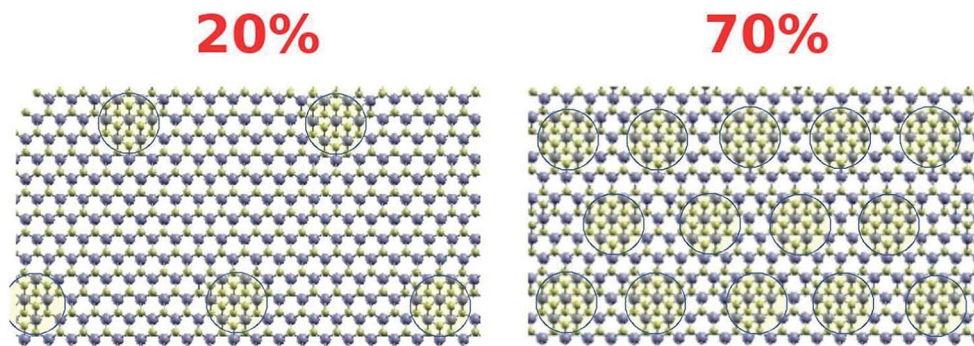| COOH	E_b (eV)	C–S (Å)	C–Mo (Å)
2H	0.20	1.87	—
1T/2H_S	1.60	1.89	—
1T/2H_Mo	0.08	—	2.68

Fig. 10 Schematic description of the density of 1T defects in both cases (20% and 70%).

as compared to S1. This observation can be correlated to the less active surface in S2 due to the smaller content of 1T phase (~20%).

Table 2 lists most of recent reports done on the dye adsorption using MoS_2. It can be noticed that our materials have shown the highest adsorption capacity for MB. In addition, in all these studies the control over the materials phase was missing and/or unknown.

3.3   Computational studies

In this part, computational studies of the adsorption properties of the hybrid MoS_2 structure was carried out with the aim to deeply understand the role of 1T active sites as well as to correlate the results with the experimental findings. Defects, edges, and other structural alterations in the MoS_2 lattice lead to active sites that can be utilized for various applications. Adsorption of dyes on MoS_2 nanosheets is mediated by the hydroxide and carboxyl groups bound to the MoS_2 surface.[21,50] It is therefore desirable to explore whether the mixed phase enhances the binding of these groups to its surface. Two MoS_2 systems were constructed, a pure 2H phase (S4), and a mixed 1T/2H phase (S1). The Mo atoms of the 1T region were marked in red (Fig. 7). Upon structural relaxation, the grain boundary found to have regions where displaced S atoms leave some Mo atoms more exposed to adsorbents compared to corresponding atoms in the pure 2H phase (Fig. 7b and c, yellow circle). Furthermore, there were sites with bonded S atoms (Fig. 7b and d, purple circle). Such structural defects present at the 1T/2H grain boundary were the focus of our computational investigation.

Fig. 8 shows the hydroxide group adsorbed on the pure 2H phase of MoS_2 (Fig. 8a), and the mixed 1T/2H phase (Fig. 8b and c). We find that the group adsorbs to the S site of the pure 2H phase with a binding energy of 1.26 eV, with an O–S distance of 1.79 Å. On the contrary, the hydroxide group adsorbs to mixed phase at the Mo site with a significantly higher energy of 2.95 eV, and an O–Mo distance of 2.09 Å, and on the S–S bonded site with an energy of 2.67 eV, and an O–S distance of 1.67 Å.

The mixed phase is also superior to the pure one in adsorbing the carboxyl group (Fig. 9), with binding energy of 1.60 eV at the S–S site, and a C–S distance of 1.89 Å. On the

contrary, the binding energy with the pure 2H phase is only 0.2 eV. Binding at the Mo site of the mixed phase is weak in this case because of the electrostatic size of the carboxyl group. Our results are summarized in Table 3.

Although we have not taken van de Waals (vdW) interactions into consideration, their effect will not significantly change our findings. vdW corrections are expected to enhance the adsorption of hydroxide and carboxyl groups on the MoS_2 surface, typically by ~0.5 eV, which will preserve the superiority of the 1T boundary regions for adsorbing the functional groups.

The density of the structural defects at the 1T grain boundaries is proportional to the perimeter of the 1T region (Fig. 10). Therefore, and assuming a fixed typical 1T size, increasing the 1T concentration will be accompanied by an increase in the adsorption capacity of the mixed phase; an increase that varies as the square root of the concentration. This is in great agreement with the maximum adsorption capacities obtained for S1 and S2. As such, an estimate of the ratio between the adsorption capacities of the 20% and 70% samples is:

$$\frac{\sqrt{70}}{\sqrt{20}} = 1.87$$

which agrees with our experimental value of this ratio = 1.8.

4.   Conclusions

Hybrid phases of MoS_2 nanosheets were prepared *via* hydrothermal method at different conditions. The adsorption performance for the MO, MB and RhB were investigated. The results indicated that the dependence of adsorption performance on 1T phase level in MoS_2 nanosheets. The superior adsorption selectivity for MB and RhB dyes over MoS_2 nanosheets is worthy noted rather than MO dye. Kinetic studies revealed that adsorption capacity of MB and RhB showed a well-fitting with the second order model with high correlation coefficient R^2. The adsorption data were fit to different isotherm models, in which the Langmuir model provided the well fit to the experimental data with maximum adsorption capacity of 787 mg g^{-1} for MB. Density functional theory calculations indicate a significantly improved adsorption performance of the

1T/2H-MoS$_2$ mixed phase, where the defects occurring at the 1T/2H grain boundaries bind the chemical groups mediating the dye adsorption more strongly.

Conflicts of interest

There are no conflicts to declare.

Acknowledgements

References

1 J. Wang, S. Han, W. Zhang, D. Liang, Y. Li, X. Zhao and R. Wang, *Int. J. Hydrogen Energy*, 2013, **38**, 14631–14637.

2 X. Mi, G. Huang, W. Xie, W. Wang, Y. Liu and J. Gao, *Carbon*, 2012, **50**, 4856–4864.

3 N. A. Travlou, G. Z. Kyzas, N. K. Lazaridis and E. A. Deliyanni, *Langmuir*, 2013, **29**, 1657–1668.

4 Y. Yu, J. Wan, Z. Yang and Z. Hu, *J. Colloid Interface Sci.*, 2017, **502**, 100–111.

5 M. R. Saber, G. Khabiri, A. A. Maarouf, M. Ulbricht and A. S. Khalil, *RSC Adv.*, 2018, **8**, 26364–26370.

6 R. Yang, J. Wang, W. Liu, Y. Zhang, H. Wang, S. Liu, Y. Guo and S. Chen, *ChemistrySelect*, 2017, **2**, 8643–8649.

7 X. Wang, J. Ding, S. Yao, X. Wu, Q. Feng, Z. Wang and B. Geng, *J. Mater. Chem. A*, 2014, **2**, 15958–15963.

8 B. A. Ali, O. I. Metwalli, A. S. Khalil and N. K. Allam, *ACS Omega*, 2018, **3**, 16301–16308.

9 B. A. Ali, A. M. Omar, A. S. G. Khalil and N. K. Allam, *ACS Appl. Mater. Interfaces*, 2019, DOI: 10.1021/acsami.9b11444.

10 Z. Zhang, P. Yang, M. Hong, S. Jiang, G. Zhao, J. Shi, Q. Xie and Y. Zhang, *Nanotechnology*, 2019, **30**, 182002.

11 U. Krishnan, M. Kaur, K. Singh, M. Kumar and A. Kumar, *Superlattices Microstruct.*, 2019, **128**, 274.

12 Y. Yu, G.-H. Nam, Q. He, X.-J. Wu, K. Zhang, Z. Yang, J. Chen, Q. Ma, M. Zhao, Z. Liu, F.-R. Ran, X. Wang, H. Li, X. Huang, B. Li, Q. Xiong, Q. Zhang, Z. Liu, L. Gu, Y. Du, W. Huang and H. Zhang, *Nat. Chem.*, 2018, **10**, 638–643.

13 A. L. Friedman, A. T. Hanbicki, F. K. Perkins, G. G. Jernigan, J. C. Culbertson and P. M. Campbell, *Sci. Rep.*, 2017, **7**, 3836.

14 D. Voiry, H. Yamaguchi, J. Li, R. Silva, D. C. Alves, T. Fujita, M. Chen, T. Asefa, V. B. Shenoy and G. Eda, *Nat. Mater.*, 2013, **12**, 850.

15 M. Li, D. Wang, J. Li, Z. Pan, H. Ma, Y. Jiang and Z. Tian, *RSC Adv.*, 2016, **6**, 71534–71542.

16 R. Abinaya, J. Archana, S. Harish, M. Navaneethan, S. Ponnusamy, C. Muthamizhchelvan, M. Shimomura and Y. Hayakawa, *RSC Adv.*, 2018, **8**, 26664–26675.

17 M. A. Lukowski, A. S. Daniel, F. Meng, A. Forticaux, L. Li and S. Jin, *J. Am. Chem. Soc.*, 2013, **135**, 10274–10277.

18 M. Acerce, D. Voiry and M. Chhowalla, *Nat. Nanotechnol.*, 2015, **10**, 313.

19 S. Bai, L. Wang, X. Chen, J. Du and Y. Xiong, *Nano Res.*, 2015, **8**, 175–183.

20 K. Chang, X. Hai, H. Pang, H. Zhang, L. Shi, G. Liu, H. Liu, G. Zhao, M. Li and J. Ye, *Adv. Mater.*, 2016, **28**, 10033–10041.

21 X.-Q. Qiao, F.-C. Hu, F.-Y. Tian, D.-F. Hou and D.-S. Li, *RSC Adv.*, 2016, **6**, 11631–11636.

22 H. Song, S. You and X. Jia, *J. Mater. Sci.: Mater. Electron.*, 2016, **27**, 10841–10848.

23 A. T. Massey, R. Gusain, S. Kumari and O. P. Khatri, *Ind. Eng. Chem. Res.*, 2016, **55**, 7124–7131.

24 B. Xu, Y. Li, G. Wang, D. Zhao, K. Pan, B. Jiang, W. Zhou and H. Fu, *Dalton Trans.*, 2015, **44**, 6224–6228.

25 H. J. Song, S. You, X. H. Jia and J. Yang, *Ceram. Int.*, 2015, **41**, 13896–13902.

26 H. Song, S. You and X. Jia, *Appl. Phys. A: Mater. Sci. Process.*, 2015, **121**, 541–548.

27 Y. Zhao, X. Zhang, C. Wang, Y. Zhao, H. Zhou, J. Li and H. Jin, *Appl. Surf. Sci.*, 2017, **412**, 207–213.

28 K.-h. HU, D.-f. ZHAO and J.-s. LIU, *Trans. Nonferrous Met. Soc. China*, 2012, **22**, 2484–2490.

29 H. Li, F. Xie, W. Li, B. D. Fahlman, M. Chen and W. Li, *RSC Adv.*, 2016, **6**, 105222–105230.

30 H. Xie and X. Xiong, *J. Environ. Chem. Eng.*, 2017, **5**, 1150–1158.

31 L. Ye, H. Xu, D. Zhang and S. Chen, *Mater. Res. Bull.*, 2014, **55**, 221–228.

32 F. Zhao, Y. Rong, J. Wan, Z. Hu, Z. Peng and B. Wang, *Nanotechnology*, 2018, **29**, 105403.

33 A. Manikandan, P. R. Ilango, C.-W. Chen, Y.-C. Wang, Y.-C. Shih, L. Lee, Z. M. Wang, H. Ko and Y.-L. Chueh, *J. Mater. Chem. A*, 2018, **6**, 15320–15329.

34 L. Kong, A. Enders, T. S. Rahman and P. A. Dowben, *J. Phys.: Condens. Matter*, 2014, **26**, 443001.

35 G. Ersan, O. G. Apul, F. Perreault and T. Karanfil, *Water Res.*, 2017, **126**, 385–398.

36 B. Szczęśniak, J. Choma and M. Jaroniec, *Adv. Colloid Interface Sci.*, 2017, **243**, 46–59.

37 F. R. Bagsican, A. Winchester, S. Ghosh, X. Zhang, L. Ma, M. Wang, H. Murakami, S. Talapatra, R. Vajtai, P. M. Ajayan, J. Kono, M. Tonouchi and I. Kawayama, *Sci. Rep.*, 2017, **7**, 1774.

38 L. Chen, E. E. L. Tanner and R. G. Compton, *Phys. Chem. Chem. Phys.*, 2017, **19**, 17521–17525.

39 F. Ferreira, A. Carvalho, Í. J. M. Moura, J. Coutinho and R. M. Ribeiro, *J. Phys.: Condens. Matter*, 2017, **30**, 035003.

40 C. González, B. Biel and Y. J. Dappe, *Phys. Chem. Chem. Phys.*, 2017, **19**, 9485–9499.

41 S.-Y. Cho, S. J. Kim, Y. Lee, J.-S. Kim, W.-B. Jung, H.-W. Yoo, J. Kim and H.-T. Jung, *ACS Nano*, 2015, **9**, 9314–9321.

42 S. S. Chou, N. Sai, P. Lu, E. N. Coker, S. Liu, K. Artyushkova, T. S. Luk, B. Kaehr and C. J. Brinker, *Nat. Commun.*, 2015, **6**, 8311.

43 D. Ghim, Q. Jiang, S. Cao, S. Singamaneni and Y.-S. Jun, *Nano energy*, 2018, **53**, 949–957.

44 L. Jiang, S. Zhang, S. A. Kulinich, X. Song, J. Zhu, X. Wang and H. Zeng, *Mater. Res. Lett.*, 2015, **3**, 177–183.

45 P. Giannozzi, S. Baroni, N. Bonini, M. Calandra, R. Car, C. Cavazzoni, D. Ceresoli, G. L. Chiarotti, M. Cococcioni, I. Dabo, A. Dal Corso, S. de Gironcoli, S. Fabris, G. Fratesi, R. Gebauer, U. Gerstmann, C. Gougoussis, A. Kokalj, M. Lazzeri, L. Martin-Samos, N. Marzari, F. Mauri, R. Mazzarello, S. Paolini, A. Pasquarello, L. Paulatto, C. Sbraccia, S. Scandolo, G. Sclauzero, A. P. Seitsonen, A. Smogunov, P. Umari and R. M. Wentzcovitch, *J. Phys.: Condens. Matter*, 2009, **21**, 395502.

46 H. J. Monkhorst and J. D. Pack, *Phys. Rev. B: Solid State*, 1976, **13**, 5188.

47 Z. Wu, B. Li, Y. Xue, J. Li, Y. Zhang and F. Gao, *J. Mater. Chem. A*, 2015, **3**, 19445–19454.

48 H. Fan, R. Wu, H. Liu, X. Yang, Y. Sun and C. Chen, *J. Mater. Sci.*, 2018, **53**, 10302–10312.

49 N. Thi Xuyen and J. M. Ting, *Chem.–Eur. J.*, 2017, **23**, 17348–17355.

50 S. Han, K. Liu, L. Hu, F. Teng, P. Yu and Y. Zhu, *Sci. Rep.*, 2017, 7, 43599.

51 V. Gupta, O. Moradi, I. Tyagi, S. Agarwal, H. Sadegh, R. Shahryari-Ghoshekandi, A. Makhlouf, M. Goodarzi and A. Garshasbi, *Crit. Rev. Environ. Sci. Technol.*, 2016, **46**, 93–118.

52 J. Fu, Z. Chen, M. Wang, S. Liu, J. Zhang, J. Zhang, R. Han and Q. Xu, *Chem. Eng. J.*, 2015, **259**, 53–61.

53 Z. Chen, J. Zhang, J. Fu, M. Wang, X. Wang, R. Han and Q. Xu, *J. Hazard. Mater.*, 2014, **273**, 263–271.

54 W. Zhang, X. Xiao, L. Zheng and C. Wan, *Can. J. Chem. Eng.*, 2015, **93**, 1594–1602.

55 X. Zhang, X. Liu, G. Liang, R. Li, H. Xu and B. Yan, *J. Quant. Spectrosc. Radiat. Transfer*, 2016, **168**, 66–77.

56 T. Yan, N. Li, Z. Qiao, W. Li, H. Wang, Z. Jing, Y. Yu and Z. Jiang, *J. Alloys Compd.*, 2019, **784**, 256–265.

57 M. T. Yagub, T. K. Sen, S. Afroze and H. M. Ang, *Adv. Colloid Interface Sci.*, 2014, **209**, 172–184.

58 M. S. Embaby, S. D. Elwany, W. Setyaningsih and M. R. Saber, *Chin. J. Chem. Eng.*, 2018, **26**, 731–739.

59 Y. Chao, W. Zhu, X. Wu, F. Hou, S. Xun, P. Wu, H. Ji, H. Xu and H. Li, *Chem. Eng. J.*, 2014, **243**, 60–67.

60 A. Pal, T. K. Jana, T. Roy, A. Pradhan, R. Maiti, S. M. Choudhury and K. Chatterjee, *ChemistrySelect*, 2018, **3**, 81–90.

61 Y. Li, H. Li, S. Zhou, H. Yang, F. Xie and W. Li, *Res. Chem. Intermed.*, 2018, **44**, 4353–4364.

62 Z. Zeng, S. Ye, H. Wu, R. Xiao, G. Zeng, J. Liang, C. Zhang, J. Yu, Y. Fang and B. Song, *Sci. Total Environ.*, 2019, **648**, 206–217.

63 S. A. Ansari, R. Kumar, M. Barakat and M. H. Cho, *J. Mater. Sci.: Mater. Electron.*, 2018, **29**, 7792–7800.